nature communications

Article | Article in Press

https://doi.org/10.1038/s41467-026-78371-6

Singularity-free supertwisted atomic layers with giant circular dichroisms

Received: 8 April 2026

Accepted: 13 September 2026

Published online: 23 October 2026

Check for updates

Xinchao Wang[1,10], Kaifeng Lin[2,3,10], Guodong Xue[2,3,10], Lifeng Hou[4], Yinghui Wei[4], Liantuan Xiao[1,5] ✉, Hao Hong[2,6] ✉, Xiaopeng Fan[1,5,7] ✉ & Kaihui Liu[2,8,9] ✉

Supertwisted van der Waals (vdW) multilayers—in which layers are stacked with identical interlayer twist angles—enable strong and programmable chiral light–matter interactions. However, directly synthesizing these multilayers remains challenging, as the conventional growth process typically produces supertwisted spirals containing an inevitable central singularity and substantial in-plane strain. Here, we demonstrate the growth of singularity-free supertwisted WS_2 multilayers by employing a dome-shaped WS_2 monolayer as a pre-deposited template. The crack line that forms on the dome acts as a dislocation line, with its two termini serving as a conjugate pair of opposite-handed screw dislocations. This configuration enables a dislocation-guided, layer-by-layer growth process that is free of topological singularities and characterized by low residual strain. The multilayers exhibit giant chiroptical responses, including a linear-optical circular dichroism (CD) of up to 10 mdeg and a second-harmonic CD of 0.81 within an ultrathin thickness of ~ 6 nm. Our work provides an effective route for growth of supertwisted multilayers and presents a programmable platform for chiral photonics.

van der Waals (vdW) materials offer unique and powerful platforms for twist-designed electronic and optical engineering processes, as their freely rotatable layers enable deterministic control over interlayer couplings and moiré potentials[1–4]. By stacking one layer onto another with a specific twist angle, the formed twisted bilayers reveal a wealth of emergent phenomena that are absent in the monolayers[5–12]. Recently, a newly opened frontier has extended the regime of twisted bilayers to supertwisted multilayers, in which each layer is stacked such that the interface maintains an identical twist angle. The supertwisted multilayers accumulate twist-induced effects along the out-of-plane direction and give rise to collective electronic and optical behaviors. Theories have predicted that a series of novel physics, such as high-order moiré superlattices[13,14], topological phase evolution trends[15], and optical activity enhancements[16], occur in supertwisted multilayers. In addition, the twist-engineered stacking scheme breaks the out-of-plane symmetry, opening pathways toward advanced applications of three-dimensional nonlinear crystals[17–21], chiral light emitters[22,23], nonvolatile memories[24,25] and polarization-programmable optical modulators[26]. However, achieving the direct growth of supertwisted multilayers with clean interfaces, scalability, and uniformity remains a longstanding challenge[27].

[1]College of Physics and Optoelectronic Engineering, Taiyuan, University of Technology, Taiyuan, Shanxi, China. [2]State Key Lab for Mesoscopic Physics and Frontiers Science Center for Nano-optoelectronics, School of Physics, Peking University, Beijing, China. [3]Academy for Advanced Interdisciplinary Studies, Peking University, Beijing, China. [4]College of Materials Science and Engineering, Taiyuan, University of Technology, Taiyuan, Shanxi, China. [5]Key Laboratory of Advanced Transducers and Intelligent Control System, Ministry of Education, Taiyuan, University of Technology, Taiyuan, Shanxi, China. [6]Interdisciplinary Institute of Light-Element Quantum Materials and Research Centre for Light-Element Advanced Materials, Peking University, Beijing, China. [7]Shanxi Key Lab of Photovoltaic Technology and Application, Taiyuan, University of Technology, Taiyuan, Shanxi, China. [8]International Centre for Quantum Materials, Collaborative Innovation Centre of Quantum Matter, Peking University, Beijing, China. [9]Songshan Lake Materials Lab, Dongguan, China. [10]These authors contributed equally: Xinchao Wang, Kaifeng Lin, Guodong Xue. ✉e-mail: xlt@sxu.edu.cn; haohong@pku.edu.cn; xiaopengfan@tyut.edu.cn; khliu@pku.edu.cn

During surface epitaxy occurring on planar substrates, thermodynamics dictates the stacking arrangement: the system preferentially adopts low-energy hexagonal or rhombohedral phases, whereas interfaces with specific twist angles correspond to high-energy metastable states[28–32]. Considerable efforts have therefore focused on kinetically perturbing the nucleation pathways and designing substrates with broken inversion symmetry to achieve these metastable chiral layers[33–39]. Recently, the most notable advance has been screw-dislocation-driven growth on curved, nonplanar substrates[40,41]. In this mechanism, the dislocation core acts as a persistent rotational source, producing a supertwisted spiral in which successive layers rotate continuously to form a helically twisted stacking sequence with a constant interlayer twist angle. However, the screw dislocation process inevitably introduces a topological singularity and generates substantial strain fields that break the in-plane C_n rotational symmetry[42]. This spatial nonuniformity distorts the moiré superlattice and the associated polarization textures, ultimately limiting the ability to explore their underlying physics and potential applications on a large scale.

A promising route for realizing singularity-free supertwisted structures is to exploit a conjugate pair of screw dislocations[43]. In principle, such a dislocation pair scheme preserves the layer-by-layer rotational stacking while avoiding the topological singularity. In practice, however, this process requires a pair of opposite-handed screw dislocations with identical twist angles, which are nucleated from spatially adjacent sites and grow at closely matched rates—conditions that are rarely satisfied in conventional growth environments. As a result, singularity-free supertwisted structures have thus far appeared very sporadically[40,43].

Here, we introduce a pre-deposited dome-shaped WS_2 monolayer as a vdW template for the synthesis of singularity-free supertwisted multilayers with geometry-dependent interlayer twist angles. The dome hosts an intrinsic crack line whose two termini naturally act as a conjugate pair of opposite-handed screw dislocations, driving layer-by-layer growth processes at matched rates. This design yields structurally independent multilayers with perfect rotational symmetry, which are free of topological singularities and exhibit low residual in-plane strain. The resulting architectures exhibit moiré-induced symmetry breaking and nonlinear geometric-phase effects, giving rise to giant linear and nonlinear circular dichroisms.

Results

Synthesis of singularity-free supertwisted WS2 multilayers

Singularity-free supertwisted WS_2 multilayers were synthesized in a tube furnace under atmospheric pressure. The key to this strategy involves the prior construction of "vdW dome" structures (Fig. 1a). Initially, the introduced deionized water reacts with the upstream WS_2 powder precursor, yielding WO_x nanoparticles. As the subsequently deposited WS_2 monolayer expands to coat these nanoparticles and form vdW dome structures, only a fraction of the WO_x is consumed, leaving a dendritic pattern beneath the monolayer (Supplementary Fig. 1). While the system reaching target temperature, the WO_x nanoparticles complete their morphological evolution and retain the dome geometry as a stable template (Supplementary Fig. 2). Within the

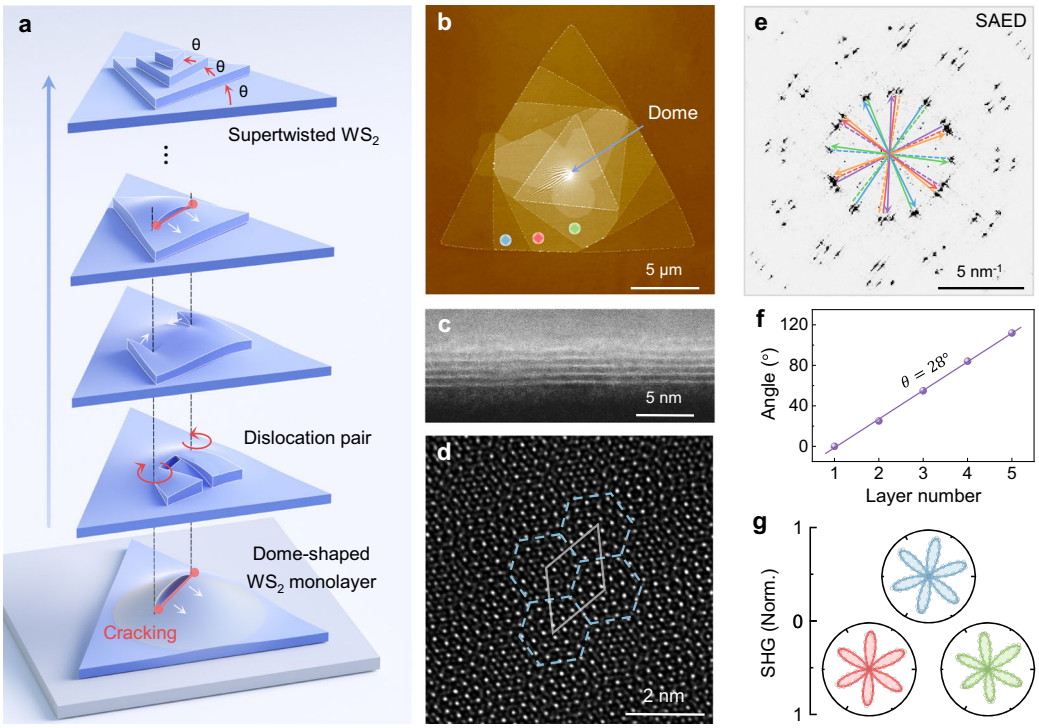


Fig. 1 | Growth process and characterization of supertwisted WS_2 multilayers. **a** A schematic illustration of the growth of supertwisted WS_2 multilayers. A crack line (red line) is located on the WS_2 dome. Two termini of the line serve as a conjugate pair of opposite-handed screw dislocations to drive the layer-by-layer growth process. θ denotes the twist angle between adjacent layers. **b** Atomic force microscopy (AFM) image of representative singularity-free supertwisted WS_2 multilayers. **c**, **d** High-angle annular dark-field scanning transmission electron microscopy (HAADF-STEM) images of the sample presented in (**b**), showing cross-sectional view (**c**) at the center, and in-plane view (**d**) of the three-layer region. The blue hexagons denote the moiré unit cells, and the white diamonds indicate moiré periods of 1.40 nm. **e** Selected-area electron diffraction (SAED) pattern acquired via STEM. Five sets of diffraction spots are obtained from a sample with a twist angle of 28° between adjacent layers. The solid lines, solid arrows and dashed lines in the same color mark the six diffraction spots from the same layer, while the colors from purple, blue, red, green, to orange distinguish the spots from the first to the fifth WS_2 layer, respectively. **f** Twist angles extracted from SAED measurements versus the number of layers. **g** Polarization-resolved second-harmonic-generation (SHG) measurements derived from selected areas in (**b**). The near-unity pattern reflects low residual in-plane strain in the singularity-free supertwisted WS_2 multilayers. Figure 1a was created using Blender 5.1 (https://www.blender.org/).

https://doi.org/10.1038/s41467-026-78371-6

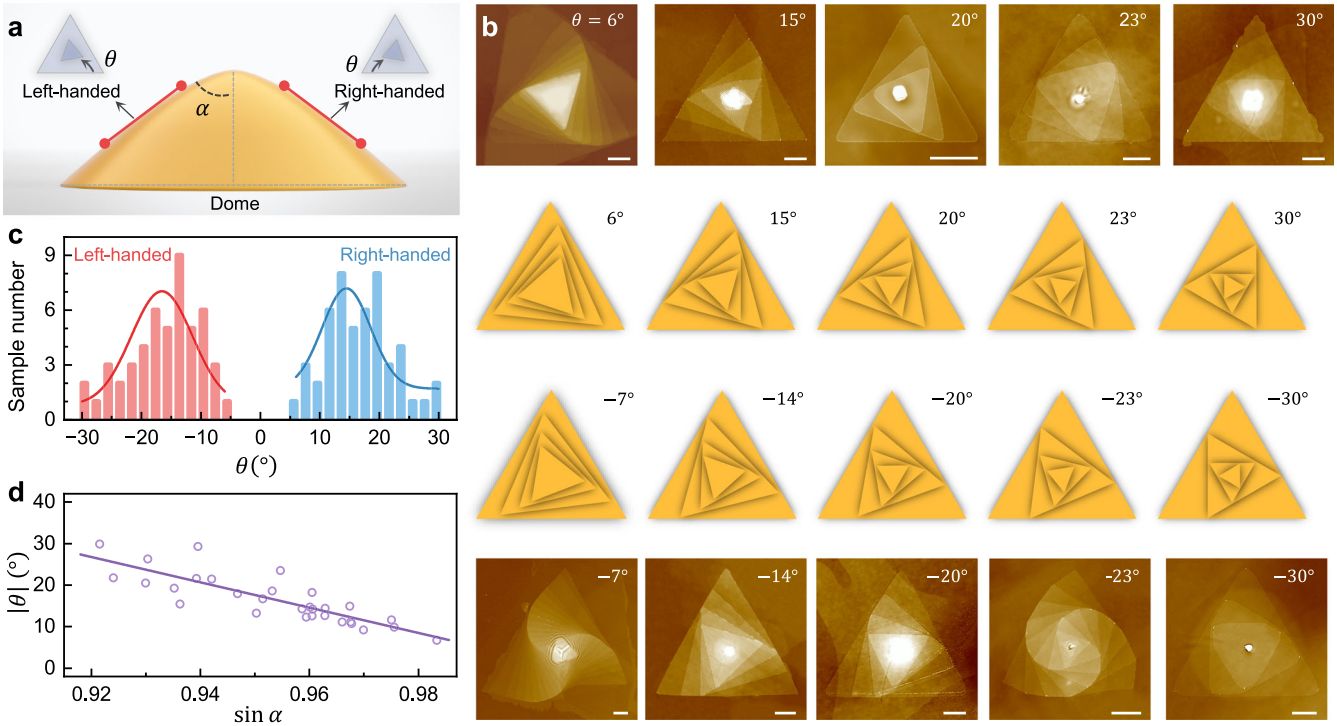


Fig. 2 | Tuneable chirality of supertwisted WS_2 multilayers. a Schematic illustration of the process for controlling the chirality in supertwisted WS_2 multilayers via the geometry of the van der Waals (vdW) dome. The handedness and twist angles are governed by the slope orientation and half-apex angle of the dome, respectively. α denotes the half-apex angle of the dome. **b** AFM images and corresponding structural illustrations of right- and left-handed WS_2 multilayers with different twist angles. Scale bars: 1 µm. **c** Histogram of the twist angles distribution observed across more than 100 samples. The solid line represents the fitted twist-angle distribution derived from the statistical data. **d** Plot of the twist angles θ as a function of the half-apex angle α of the dome. The solid line denotes the fitted dependence of θ on sin α. Figure 2a was created using Blender 5.1 (https://www.blender.org/).

dome, the two-dimensional lattice tears because of the adaptation of three-dimensional structures, resulting in the formation of a crack line[44].

The two termini of the crack line anchor into the crystal lattice, creating a Frank–Read source[45]. The Frank–Read source serves as a nucleation site, forming a pair of conjugate opposite-handed spiral arms. These arms grow outward while moving towards each other, eventually meeting and coalescing to produce a closed loop that constitutes singularity-free WS_2 lattices (Supplementary Fig. 3). The Frank–Read source acts as an active growth front, repeatedly expanding around the dome surface, with each complete growth cycle depositing an additional layer. Each layer undergoes a rotational process to accommodate the inherent geometric angular deficit (θ) of the dome, resulting in the stepwise accumulation of a precisely supertwisted structure through layer-by-layer stacking (Supplementary Fig. 4). The formation of vdW domes is a prerequisite for the generation of singularity-free supertwisted WS_2 multilayers, distinguishing this mechanism from the formation of supertwisted spiral structures on Si/SiO_2 substrates (Supplementary Fig. 5).

A representative supertwisted WS_2 multilayer composed of five distinct triangular layers is shown in Fig. 1b. The edge-closed triangular morphology highlights the singularity-free twisted stacking configuration, contrasting with spiral-type structures (Supplementary Fig. 6). This edge-closed structure is topologically singularity-free because the conjugate screw-dislocation pair drives oppositely spiral steps that merge at the edges, allowing the generated layers to stitch into closed triangular loops. To resolve its atomic-scale structure, high-angle annular dark-field scanning transmission electron microscopy (HAADF-STEM) is performed. In the out-of-plane view at the center of the triangular sample, a well-ordered atomic arrangement scheme is observed, with each WS_2 layer maintaining structural independence (Fig. 1c). The in-plane view exhibits a prominent moiré pattern that evolves systematically with the number of layers, indicating high crystalline quality (Fig. 1d and Supplementary Fig. 7). Furthermore, selected-area electron diffraction (SAED) patterns derived from the five-layer region (Fig. 1e) reveal five distinct sets of diffraction spots, each corresponding to an individual WS_2 layer. These patterns demonstrate uniform interlayer twist angles, confirming the successful synthesis of supertwisted structures (Fig. 1f). Additionally, polarization-resolved second-harmonic-generation (SHG) measurements are obtained at different sample positions. The near-unity intensity modulation exhibited by the six-petal SHG pattern directly indicates the nearly preserved in-plane C_3 rotational symmetry (Fig. 1g and Supplementary Fig. 8)[46].

Tuneable chirality of supertwisted WS2 multilayers

The spatial position of the dislocation line on the vdW dome, together with the geometric parameters of the dome, directly determines the chirality——specifically the handedness and twist angles——of the resulting WS_2 multilayer structure (Fig. 2a). In the growth direction indicated in Fig. 1a, a dislocation line situated on the left side of the dome produces a left-handed chiral structure, whereas a line on the right side yields a right-handed chiral structure (Supplementary Fig. 9). At the same time, the three-dimensional dome inherently brings an angular deficit for the growth of two-dimensional materials because of lattice match. This angular deficit can be precisely tuned via the half-apex angle α of the dome (Supplementary Fig. 10).

Experimentally, we synthesized extensive supertwisted WS_2 samples with different handedness (Fig. 2b). Representative atomic force microscopy (AFM) images reveal distinct right- and left-handed structures (labeled "+" and "-", respectively) with lateral dimensions of approximately 10 µm. A statistical analysis of more than 100 samples

demonstrates that the interlayer twist angles can be accessed over a continuous range from −30° to +30° (Fig. 2c, Supplementary Figs. 11 and 12). Through a correlation analysis between the half-apex angle α of the dome and the measured interlayer twist angles θ, we establish a geometric relationship of $|\theta| = 2\pi(1 - \sin\alpha)$, which agrees well with our Frank–Read source growth mechanism (Fig. 2d).

Linear chiroptical responses in supertwisted multilayers

The supertwisted architecture endows WS_2 multilayers with unique chiral light–matter interaction characteristics: the interplay between interlayer electronic coupling and moiré superlattice periodicity reshapes their excitonic fine structure, whereas the twist-induced geometry breaks both the inversion and mirror symmetries. Thus, supertwisted WS_2 multilayers serve as a promising platform for chiroptical and optoelectronic applications with pronounced linear and nonlinear circular dichroism (CD) (Fig. 3a).

To quantify the linear CD of supertwisted WS_2 multilayers, we develop a high-sensitivity CD spectroscopy system, as shown in Fig. 3b[47]. In the system, the excitation laser is alternately modulated by a photoelastic modulator (PEM) operating at 50 kHz, generating left- and right-handed circularly polarized (LCP and RCP, respectively) light. The differential absorption of supertwisted WS_2 is recorded via a lock-in amplifier, which simultaneously captures the time-varying signal (I_{AC}) and the average signal (I_{DC}) (Fig. 3c). The optical activity is then defined as CD=I_{AC}/I_{DC}.

The wavelength-dependent absorption (top), linear CD (middle) and optical rotatory dispersion (ORD) (bottom) spectra of a supertwisted WS_2 multilayer are shown in Fig. 3d. The absorption spectrum exhibits pronounced peaks at approximately 630, 525 and 455 nm, corresponding to the A-, B- and C- excitons, respectively, of WS_2. In the linear CD spectrum, an apparent Cotton effect emerges near these excitonic resonances, where the CD signal reverses its sign across the absorption maxima and develops a derivative-like profile (Fig. 3d and Supplementary Figs. 13–15). Moreover, enantiomers with opposite stacking handedness exhibit similar excitonic absorption features but sign-reversed CD responses (Supplementary Fig. 15). A maximum CD value of 9.6 mdeg is obtained around the C-exciton at 460 nm. In addition to the chiral absorption effect, the intrinsic chirality of the supertwisted architecture also imparts phase retardation to the transmitted light, which is described by the real parts of the refractive index. Guided by the Kramers–Kronig relations, the optical rotatory dispersion spectrum is derived from the CD data (Fig. 3d, bottom; Supplementary Note 1). It exhibits a similar resonant trend, reaching a maximum of −7.3 mdeg near the C-exciton.

Nonlinear chiroptical responses of supertwisted multilayers

In the following section, we discuss the nonlinear SHG-CD of supertwisted WS_2 multilayers. Under circularly polarized light excitation, the SHG electric field derived from θ-twisted WS_2 can be expressed as follows (Supplementary Note 2).

$$\begin{aligned} \boldsymbol{E}_{2\omega}^{+} &= \frac{\sqrt{2}\omega}{cn(2\omega)}\chi^{(2)} \cdot \boldsymbol{E}_{\omega}^{-2}\left(\frac{1-e^{-i\triangle kt}}{\triangle k}\cdot\frac{1-e^{-iN(\triangle kt+3\theta)}}{1-e^{-i(\triangle kt+3\theta)}}\right) \\ \boldsymbol{E}_{2\omega}^{-} &= \frac{\sqrt{2}\omega}{cn(2\omega)}\chi^{(2)} \cdot \boldsymbol{E}_{\omega}^{+2}\left(\frac{1-e^{-i\triangle kt}}{\triangle k}\cdot\frac{1-e^{-iN(\triangle kt-3\theta)}}{1-e^{-i(\triangle kt-3\theta)}}\right) \end{aligned} \quad (1)$$

Thus, the SHG-CD is derived to be:

$$CD_{\mathrm{SHG}} = \frac{S(\varphi_+) - S(\varphi_-)}{S(\varphi_+) + S(\varphi_-)} \quad (2)$$

with

$$S(\varphi_\pm) = \frac{\sin^2\left(\frac{N\varphi_\pm}{2}\right)}{\sin^2\left(\frac{\varphi_\pm}{2}\right)}, \varphi_\pm = \triangle kt \pm 3\theta.$$

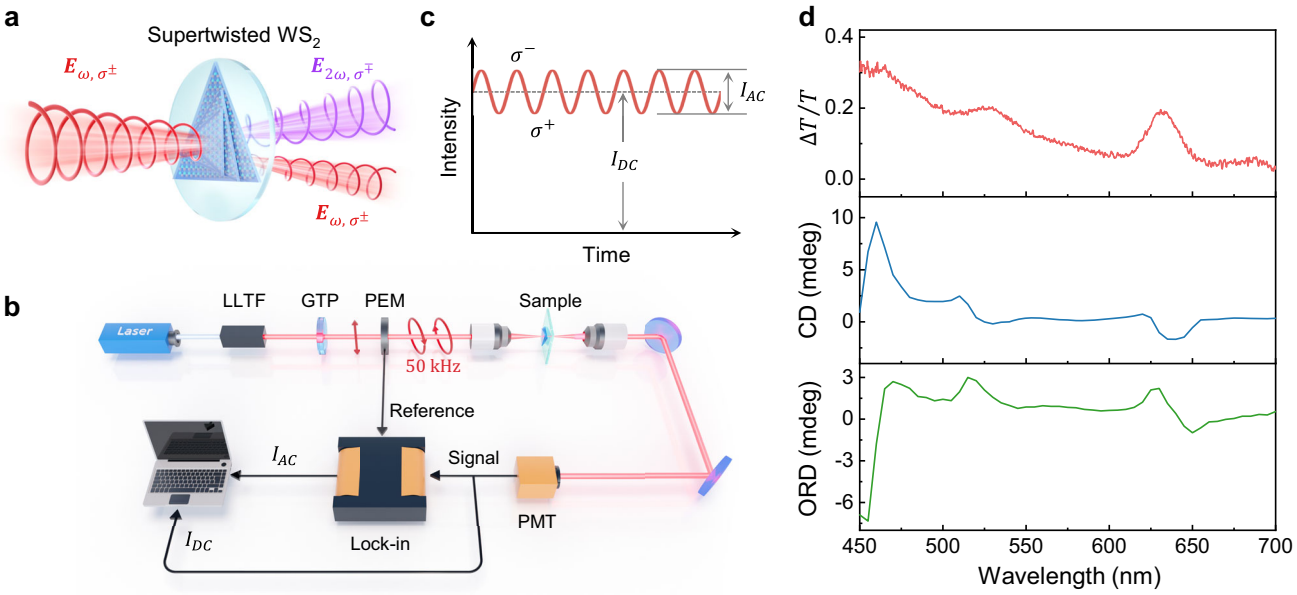


Fig. 3 | Linear chiroptical responses of supertwisted WS_2 multilayers. **a** Schematic diagram of the linear and nonlinear optical responses of supertwisted WS_2 multilayers. $E_{\omega,\sigma^\pm}$ denotes the electric field of the fundamental light at frequency ω with right- or left-circular polarization, respectively, whereas $E_{2\omega,\sigma^\mp}$ denotes the electric field of the generated second-harmonic signal at frequency 2ω with left- or right-circular polarization. **b** Schematic of the absorption–circular dichroism (CD) experimental setup. SC Supercontinuum laser; LLTF Laser line-tunable optical filter; GTP Glan-Taylor polarizer; PEM Photoelastic modulator; PMT Photomultiplier tube. **c** Simplified diagram of the absorption–CD setup over time, containing the average signal (I_{DC}) and the time-varying signal (I_{AC}) with alternating circularly polarized incident light. **d** Differential transmission spectroscopy (top), linear absorption–CD spectroscopy (middle), and optical rotatory dispersion (ORD) spectrum (bottom) of supertwisted WS_2 multilayers. The sample has a twist angle $\theta = 14^\circ$ and $N = 6$ layers. Figure 3a, b were created using Blender 5.1 (https://www.blender.org/).

Here ω is the frequency of the fundamental light, c is the velocity of light in vacuum, $n(2\omega)$ is the refractive index of the second-harmonic (SH) light, χ is the second-order susceptibility of WS_2, $\boldsymbol{E}_{\omega}^{\mp 2}$ is the electric field of left- and right-circularly polarized fundamental light, $\triangle k = k_{2\omega} - 2k_{\omega}$ is the wavevector mismatch between the fundamental and SH light, t is the monolayer thickness, 3θ is the nonlinear geometric phase introduced by the twist angles θ, and N is the total number of layers.

The complex-amplitude diagram of the SHG electric fields is shown in Fig. 4a, revealing the coherent superposition of nonlinear polarizations derived from sequentially twisted layers. The $\boldsymbol{E}_{2\omega}^{+}$ and $\boldsymbol{E}_{2\omega}^{-}$ vectors evolve along circular trajectories in the complex plane, with diameters proportional to $\left|1-e^{-i(\triangle kt+3\theta)}\right|^{-1}$ and $\left|1-e^{-i(\triangle kt-3\theta)}\right|^{-1}$, respectively. The ratio of the circular trajectory to the full circumference is given by $\frac{N\triangle kt}{\pi}$. Guided by this framework, we demonstrate precise control over the SHG-CD by tuning N and θ. The SHG spectra obtained for supertwisted WS_2 multilayers with $N = 8$ and $\theta = 5^{\circ}$ under LCP and RCP excitations are shown in Fig. 4b. A noticeable SHG intensity difference is observed, with the SHG-CD, defined as $\frac{(I_{2\omega}^{+}-I_{2\omega}^{-})}{(I_{2\omega}^{+}+I_{2\omega}^{-})}$, determined to be 0.67.

Furthermore, by tuning the excitation wavelength and number of layers, the two-dimensional plots of the SHG-CD acquired from our experiment are shown in Fig. 4c. The SHG-CD can be continuously tuned from −0.81 to 0.61, and this range is in close agreement with that of our theoretical model (Fig. 4d). To facilitate a clear comparison, two representative cross-sections are extracted: the pink dashed line corresponds to the wavelength-dependent SHG-CD spectra at $N = 8$ (Fig. 4e), whereas the purple dashed line corresponds to the layer number-dependent SHG-CD evolution trend at $\lambda_{SHG} = 480$ nm (Fig. 4f). The wavelength dependence of the SHG-CD is pronounced because of the chromatic dispersion effect and the associated variation in $\triangle k$. At 320 nm, the SHG-CD reaches a negative maximum value of -0.81. With increasing wavelength, this value decreases and undergoes an abrupt transition from negative to positive near 410 nm as $\triangle k$ changes from negative to positive (Supplementary Fig. 16). Afterwards, it increases to a positive maximum of 0.6 at 480 nm (Fig. 4e). However, the layer number-dependent SHG-CD increases progressively within 10 layers, approaching 0.61 for $N = 10$ at $\lambda_{SHG} = 480$ nm in our experiments (Fig. 4f).

Discussion

In summary, this work demonstrates a reliable strategy for synthesizing singularity-free supertwisted vdW multilayers by designing a predeposited WS_2 monolayer dome as a template. The dome supplies a conjugate pair of screw dislocations that merge two opposite-handed spirals, thereby yielding a singularity-free structure during the growth process. The resulting structures exhibit accumulated twist-induced chiroptical effects, leading to pronounced linear and nonlinear CD. This work establishes a paradigm for producing chiral two-dimensional vdW materials that retain their intrinsic symmetries and properties. Such supertwisted systems offer versatile platforms for exploring chiral photonic, electronic, and optoelectronic technologies.

Methods

Growth of singularity-free supertwisted WS2 multilayers

A water-assisted chemical vapor deposition (CVD) approach was employed to synthesize supertwisted WS_2 multilayers. The entire synthesis was conducted in a horizontal tube furnace (Nanjing Boyuntong Instrument). The results are characterized by the Micro-

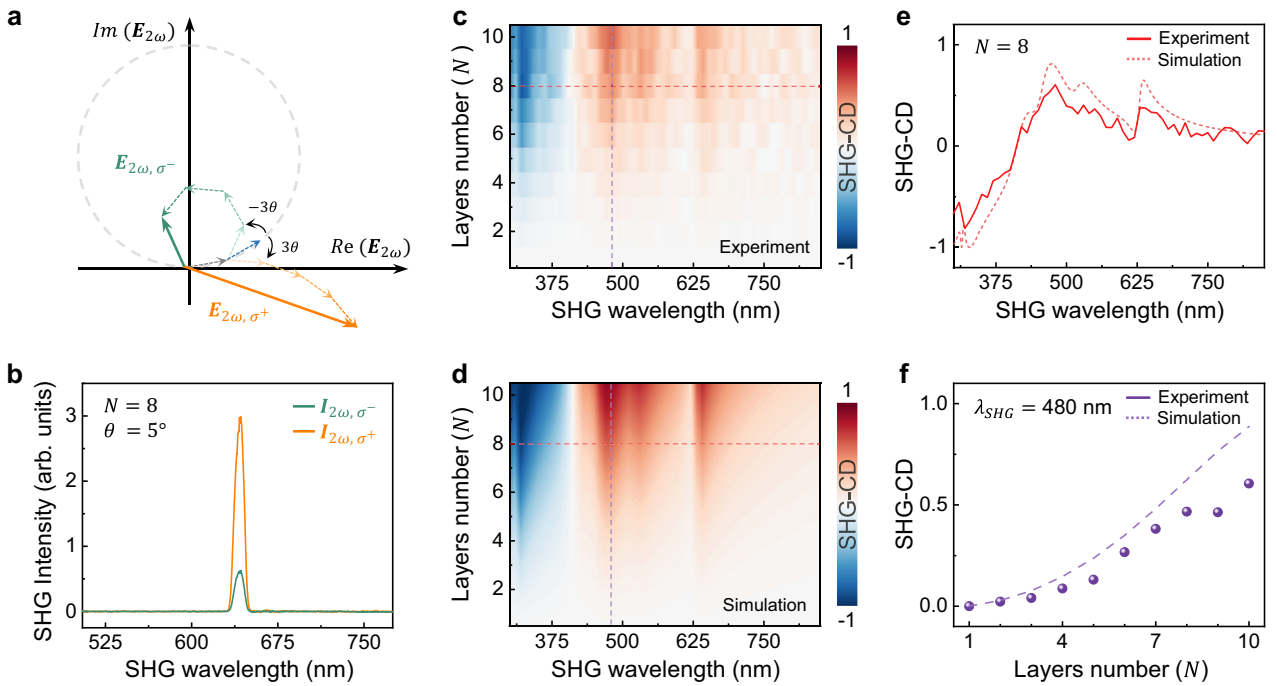


Fig. 4 | Nonlinear chiroptical responses of supertwisted WS_2 multilayers. **a** Complex-amplitude diagram illustrating the processes of generating left (σ^-) and right (σ^+) circularly polarized SHG electric fields. The gray dashed arrow indicates the SHG from the first layer, whereas the blue dashed arrow corresponds to the second layer without rotation. The green (orange) dashed arrows represent successive σ^-(σ^+) polarized SHG contributions with an interlayer twist angle of θ, whose vectorial summation yields the resultant SHG field shown as the solid green (orange) arrow. The difference between the two resultant fields gives rise to the SHG-CD. **b** SHG spectra of an 8-layer supertwisted WS_2 sample with a 5° twist angle, exhibiting a pronounced SHG-CD of 0.67. **c**, **d** Broadband SHG layer-dependent mapping diagrams derived from the experimental measurements (c) and the theoretical simulation (**d**). **e** Wavelength-dependent SHG-CD. The SHG-CD evolves with the SHG wavelength, approaching a maximum of −0.81 at 320 nm. Dashed line: simulation from (**d**); solid line: experimental data from (**c**). **f** Layer number-dependent SHG-CD, revealing a monotonic increase as the number of layers increases. Dashed line: theoretical prediction derived from (**d**); dots: experimental data from (**c**).

STS1200 system (Units Technology, www.units-tech.com.cn). The Si/SiO_2 substrate was ultrasonically cleaned with acetone, isopropanol, and deionized water, dried with nitrogen gas, and positioned 7–10 cm downstream from the center of the tube furnace. 100 mg of WS_2 precursor powder (Alfa Aesar, 99.8%) in an alumina boat was placed in the central zone. 30–50 µL of deionized water in an alumina boat was placed upstream (15–18 cm) in a lower-temperature region. The system was initially purged with argon (Ar) at a flow rate of 200 sccm for 30 min, after which the Ar flow was reduced to 80 sccm to act as the carrier gas. The central zone temperature was raised from room temperature to 1000 °C at 30 °C/min. After the first stage, the introduction of water vapor was stopped, and the temperature of the central zone was increased from 1000 °C to 1150 °C at a rate of 30 °C/min without changing the gas flow. The peak temperature was maintained for 5–10 min. Finally, the sample was allowed to cool down to room temperature under flowing argon.

AFM characterizations
AFM data were acquired with Bruker Multimode 8.

STEM characterizations
As-grown WS_2 multilayers on Si/SiO_2 substrates were transferred to a 250 mesh Cu grid using the wet transfer method. The substrate was spin-coated with a poly methyl methacrylate (PMMA A4) at 5000 rpm/min and baked at 150 °C for 15 min. The PMMA/WS_2 composites were immersed in 3 mol/L NaOH solution to detach the PMMA/WS_2 composite from the Si/SiO_2 substrate at room temperature. The PMMA/WS_2 film was then transferred onto the grid. The grid was then placed over acetone vapor for 30 min to remove the PMMA. High-resolution STEM observations were done on an aberration-corrected JEOL JEM-ARM300F2 under 300 kV, equipped with a double spherical aberration corrector and K3 direct electronic camera. A 53 mrad convergence angle was used for high-angle annular dark-field image acquisition.

Linear absorption-CD measurements
Monochromatic wavelength selection was achieved using a laser line filter (NKT Photonics, SuperK SELECT) coupled to a supercontinuum laser source (NKT Photonics, SuperK EXTREME). For each selected wavelength, left- and right-handed circularly polarized light states were generated at 50 kHz using a Glan-Taylor polarizer (Thorlabs, GTH10M) combined with a photoelastic modulator (Hinds Instruments, PEM100). The modulated beam was focused onto supertwisted WS_2 multilayers through a 100× objective (Olympus MPLFLN100X Objective, NA = 0.90), with chiral signals collected in the transmission mode by a 100× objective (Mitutoyo Plan Apo NIR Infinity Corrected Objective, NA = 0.50) in a confocal geometry. Signal detection employed a photon-counting photomultiplier module (Thorlabs, PMT1001/M) synchronized with a lock-in amplifier (Zurich Instruments, HF2LI) referenced to the PEM frequency. This configuration enabled simultaneous acquisition of the time-varying AC component (I_{AC}) and the average DC intensity (I_{DC}). Spectral circular dichroism (CD) mapping (450–700 nm, 5 nm resolution) was performed by synchronizing wavelength scanning with lock-in detection.

SHG measurements
A supercontinuum laser source (NKT Photonics, SuperK EXTREME) was used as the laser system for broadband SHG measurement. A mode-locked Ti:sapphire oscillator (Coherent Mira-HP, ~130 fs, 76 MHz) equipped with an optical parametric oscillator (Coherent Mira-OPO-X) was used as the laser system for single wavelength SHG measurement. The excitation laser beam was focused using a 100× objective (Olympus MPLFLN100X Objective, NA = 0.90), and its polarization was controlled by a Superachromatic Quarter-Wave Plate (Thorlabs, SAQWP05M-1700). The generated circularly polarized light was calibrated using a Thorlabs polarimeter (PAX1000IR2). The SHG signals were collected in the transmission mode by a 100× objective (Mitutoyo Plan Apo NIR Infinity Corrected Objective, NA = 0.50) in a confocal geometry. After filtering out the excitation laser, the SHG signal was recorded using a spectrometer equipped with a thermoelectric cooling CCD camera (Andor DU420A-BU2).

Data availability
The Source Data underlying the figures of this study are available with the paper. All raw data generated during the current study are available from the corresponding authors upon request. Source data are provided with this paper.

References

1. Wilson, N. P., Yao, W., Shan, J. & Xu, X. Excitons and emergent quantum phenomena in stacked 2D semiconductors. *Nature* **599**, 383–392 (2021).
2. Huang, D., Choi, J., Shih, C.-K. & Li, X. Excitons in semiconductor moiré superlattices. *Nat. Nanotechnol.* **17**, 227–238 (2022).
3. Mak, K. F. & Shan, J. Semiconductor moiré materials. *Nat. Nanotechnol.* **17**, 686–695 (2022).
4. Du, L. et al. Moiré photonics and optoelectronics. *Science* **379**, eadg0014 (2023).
5. Cao, Y. et al. Unconventional superconductivity in magic-angle graphene superlattices. *Nature* **556**, 43–50 (2018).
6. Tran, K. et al. Evidence for moiré excitons in van der Waals heterostructures. *Nature* **567**, 71–75 (2019).
7. Wang, X. et al. Light-induced ferromagnetism in moiré superlattices. *Nature* **604**, 468–473 (2022).
8. Ma, C. et al. Intelligent infrared sensing enabled by tunable moiré quantum geometry. *Nature* **604**, 266–272 (2022).
9. Tsang, C. S. et al. Polar and quasicrystal vortex observed in twisted-bilayer molybdenum disulfide. *Science* **386**, 198–205 (2024).
10. Li, Y. et al. Tuning commensurability in twisted van der Waals bilayers. *Nature* **625**, 494–499 (2024).
11. Zheng, X. et al. Twist-assisted intrinsic toughening in two-dimensional transition metal dichalcogenides. *Nat. Mater.* **24**, 1561–1568 (2025).
12. Zhang, F. et al. Experimental signature of layer skyrmions and implications for band topology in twisted WSe_2 bilayers. *Nat. Phys.* **21**, 1217–1223 (2025).
13. Ji, Z. et al. Opto-twistronic Hall effect in a three-dimensional spiral lattice. *Nature* **634**, 69–73 (2024).
14. Park, D. et al. Unconventional domain tessellations in moiré-of-moiré lattices. *Nature* **641**, 896–903 (2025).
15. Wu, F., Zhang, R.-X. & Das Sarma, S. Three-dimensional topological twistronics. *Phys. Rev. Res.* **2**, 022010 (2020).
16. Wang, Y.-Q., Morimoto, T. & Moore, J. E. Optical rotation in thin chiral/twisted materials and the gyrotropic magnetic effect. *Phys. Rev. B* **101**, 174419 (2020).
17. Hong, H. et al. Twist phase matching in two-dimensional materials. *Phys. Rev. Lett.* **131**, 233801 (2023).
18. Tang, H. et al. On-chip multi-degree-of-freedom control of two-dimensional materials. *Nature* **632**, 1038–1044 (2024).
19. Kim, B. et al. Three-dimensional nonlinear optical materials from twisted two-dimensional van der Waals interfaces. *Nat. Photonics* **18**, 91–98 (2024).
20. Ma, C. et al. Phase matching of high harmonic generation in twisted van der Waals crystals. *Phys. Rev. Lett.* **135**, 166902 (2025).
21. Lin, K. et al. Nonlinear phase-matched van der Waals crystals integrated on optical fibres. *Nat. Mater.* **25**, 581–587 (2026).
22. Kim, C.-J. et al. Chiral atomically thin films. *Nat. Nanotechnol.* **11**, 520–524 (2016).
23. Enders, M. T. et al. Mid-infrared chirality and chiral thermal emission from twisted α-MoO_3. *Nat. Commun.* **16**, 11086 (2025).

24. Yasuda, K., Wang, X., Watanabe, K., Taniguchi, T. & Jarillo-Herrero, P. Stacking-engineered ferroelectricity in bilayer boron nitride. *Science* **372**, 1458–1462 (2021).
25. Vizner Stern, M. et al. Interfacial ferroelectricity by van der Waals sliding. *Science* **372**, 1462–1466 (2021).
26. Dai, D. et al. Twist angle–dependent valley polarization switching in heterostructures. *Sci. Adv* **10**, eado1281 (2024).
27. Li, J. et al. Towards the scalable synthesis of two-dimensional heterostructures and superlattices beyond exfoliation and restacking. *Nat. Mater.* **23**, 1326–1338 (2024).
28. Liu, K. et al. Evolution of interlayer coupling in twisted molybdenum disulfide bilayers. *Nat. Commun.* **5**, 4966 (2014).
29. He, J., Hummer, K. & Franchini, C. Stacking effects on the electronic and optical properties of bilayer transition metal dichalcogenides MoS_2, $MoSe_2$, WS_2, and WSe_2. *Phys. Rev. B* **89**, 075409 (2014).
30. Li, X. et al. Rhombohedral-stacked bilayer transition metal dichalcogenides for high-performance atomically thin CMOS devices. *Sci. Adv* **9**, eade5706 (2023).
31. Qin, B. et al. Interfacial epitaxy of multilayer rhombohedral transition-metal dichalcogenide single crystals. *Science* **385**, 99–104 (2024).
32. Liu, L. et al. Homoepitaxial growth of large-area rhombohedral-stacked MoS_2. *Nat. Mater.* **24**, 1195–1202 (2025).
33. Sun, L. et al. Hetero-site nucleation for growing twisted bilayer graphene with a wide range of twist angles. *Nat. Commun.* **12**, 2391 (2021).
34. Liu, C. et al. Designed the growth of large bilayer graphene with arbitrary twist angles. *Nat. Mater.* **21**, 1263–1268 (2022).
35. Xu, M. et al. Reconfiguring nucleation for CVD growth of twisted bilayer MoS_2 with a wide range of twist angles. *Nat. Commun.* **15**, 562 (2024).
36. Xu, M. et al. CVD synthesis of twisted bilayer WS_2 with tunable second harmonic generation. *Adv. Mater.* **36**, 2313638 (2024).
37. Fortin-Deschênes, M., Watanabe, K., Taniguchi, T. & Xia, F. Van der Waals epitaxy of tunable moirés enabled by alloying. *Nat. Mater.* **23**, 339–346 (2024).
38. Zhou, J. et al. Homo-site nucleation growth of twisted bilayer MoS_2 with commensurate angles. *Adv. Mater.* **36**, 2408227 (2024).
39. Li, X. et al. Controlling twisted angles in directly grown MoS_2 bilayers via tilt grain boundary engineering. *Adv. Sci.* **12**, e09280 (2025).
40. Zhao, Y. et al. Supertwisted spirals of layered materials enabled by growth on non-Euclidean surfaces. *Science* **370**, 442–445 (2020).
41. Chen, J. et al. Structure-dependent nonlinear optical effects in spiral WS_2 nanosheets. *Adv. Mater.* **37**, 2415214 (2025).
42. Ci, P. et al. Breaking rotational symmetry in supertwisted WS_2 spirals via moiré magnification of intrinsic heterostrain. *Nano Lett.* **22**, 9027–9035 (2022).
43. Wang, Z.-J. et al. Conversion of chirality to twisting via sequential one-dimensional and two-dimensional growth of graphene spirals. *Nat. Mater.* **23**, 331–338 (2024).
44. Vitelli, V., Lucks, J. B. & Nelson, D. R. Crystallography on curved surfaces. *Proc. Natl. Acad. Sci.* **103**, 12323–12328 (2006).
45. Frank, F. C. & Read, W. T. Multiplication processes for slow-moving dislocations. *Phys. Rev.* **79**, 722–723 (1950).
46. Mennel, L. et al. Optical imaging of strain in two-dimensional crystals. *Nat. Commun.* **9**, 516 (2018).
47. Yao, F. et al. Complete structural characterization of single carbon nanotubes by Rayleigh scattering circular dichroism. *Nat. Nanotechnol.* **16**, 1073–1078 (2021).

Acknowledgments

The authors acknowledge the assistance of the Center for Analytical Testing and Instrument Sharing of Taiyuan University of Technology.

Author contributions

X.F. and K.H.L. supervised the project. X.F., K.H.L., H.H. and L.X. conceived and coordinated the experiments. X.W., G.X. and X.F. developed the growth mechanism. X.W., L.H. and Y.W. conducted the growth experiments. K.F.L. performed the optical experiments and theoretical calculations. All the authors discussed the results and revised the paper.

Funding

This work was supported by the National Natural Science Foundation of China (52273252 (X.P.F.), 92577201 (K.H.L.), 42550189 (K.H.L.), 12422406 (H.H.), U23A20380 (L.T.X.), U24A6002 (L.F.H.)), National Key R&D Program of China (2022YFA1403504 (K.H.L.), 2022YFA140420 (L.T.X.)), Guangdong Major Project of Basic and Applied Basic Research (2021B0301030002 (K.H.L.)). Research Project Supported by Shanxi Scholarship Council of China.

Competing interests

The authors declare no competing interests.

Additional information

Supplementary information The online version contains supplementary material available at https://doi.org/10.1038/s41467-026-78371-6.

Correspondence and requests for materials should be addressed to Liantuan Xiao, Hao Hong, Xiaopeng Fan or Kaihui Liu.

Peer review information *Nature Communications* thanks Cheol-Joo Kim, Ye Wang, and the other anonymous reviewer(s) for their contribution to the peer review of this work. A peer review file is available.

Reprints and permissions information is available at http://www.nature.com/reprints

Publisher's note Springer Nature remains neutral with regard to jurisdictional claims in published maps and institutional affiliations.

Open Access This article is licensed under a Creative Commons Attribution-NonCommercial-NoDerivatives 4.0 International License, which permits any non-commercial use, sharing, distribution and reproduction in any medium or format, as long as you give appropriate credit to the original author(s) and the source, provide a link to the Creative Commons licence, and indicate if you modified the licensed material. You do not have permission under this licence to share adapted material derived from this article or parts of it. The images or other third party material in this article are included in the article's Creative Commons licence, unless indicated otherwise in a credit line to the material. If material is not included in the article's Creative Commons licence and your intended use is not permitted by statutory regulation or exceeds the permitted use, you will need to obtain permission directly from the copyright holder. To view a copy of this licence, visit http://creativecommons.org/licenses/by-nc-nd/4.0/.

© The Author(s) 2026

This Article in Press is shared early to give you faster access to new research. It is citable and carries a permanent DOI. The final edited version will replace it automatically.